Korean J. Chem. Eng., **27**(1), 355-363 (2010)
DOI: 10.1007/s11814-009-0321-5

Numerical and experimental investigation of a fluidized bed chamber hydrodynamics with heat transfer

Mahdi Hamzehei*,† and Hassan Rahimzadeh**

*Department of Mechanical Engineering, Islamic Azad University, Ahwaz Branch, Ahwaz, Iran
**Fluid Mechanics Research Center, Department of Mechanical Engineering,
Amirkabir University of Technology (Tehran Polytechnics), No. 424, Hafez Avenue, Tehran 15875-4413, Iran
(*Received 6 March 2009 • accepted 30 June 2009*)

Abstract−The hydrodynamics and heat transfer of a gas-solid fluidized bed chamber was investigated by computational fluid dynamic (CFD) techniques. A multifluid Eulerian model incorporating the kinetic theory for solid particles was applied to simulate the unsteady state behavior of this chamber. For momentum exchange coefficients, Syamlal-O'Brien drag functions were used. A suitable numerical method that employed finite volume method was applied to discretize the equations. The simulation results also indicated that small bubbles were produced at the bottom of the bed. These bubbles collided with each other as they moved upwards forming larger bubbles. Also, the solid particle temperature effect on heat transfer and hydrodynamics was studied. Simulation results were compared with the experimental data in order to validate the CFD model. Pressure drops and mean gas temperature predicted by the simulations at different positions in the chamber were in good agreement with experimental measurements at gas velocities higher than the minimum fluidization velocity. Furthermore, this comparison showed that the model could predict hydrodynamics and heat transfer behaviors of gas solid fluidized bed reasonably well.

Key words: CFD, Experimental, Fluidized Bed, Hydrodynamics, Gas-solid Flow

INTRODUCTION

Fluidized bed reactors are used in a wide range of applications in various industrial operations, including chemical, mechanical, petroleum, mineral, and pharmaceutical industries. Understanding the heat transfer and hydrodynamics of fluidized bed reactors is essential for choosing the correct operating parameters for the appropriate fluidization regime [1]. Computational fluid dynamics (CFD) offers an approach to understanding the complex phenomena that occur between the gas phase and the particles. The Eulerian-Lagrangian and Eulerian-Eulerian models have been applied to the CFD modeling of multiphase systems. To model gas-solid flows, usually, the Eulerian-Lagrangian are called discrete particle models (DPM), and Eulerian-Eulerian models are called granular flow models. Granular flow models (GFM) are continuum-based and are more suitable for simulating large and complex industrial fluidized bed reactors containing billions of solid particles. These models, however, require information about solid phase rheology and particle-particle interaction laws. In principle, discrete phase models (DPM) can supply such information.

DPMs in turn need closure laws to model fluid-particle interactions and particle-particle interaction parameters based on contact theory and material properties.

In principle, it is possible to work on way upwards from direct solution of Navier-Stokes equations [2,3]. Lattice-Boltzmann models and contact theory obtain all the necessary closure laws and other parameters required for granular flow models. Direct solution of Navier-Stokes equations or lattice Boltzmann methods is too computation intensive to simulate even thousands of solid particles. Rather than millions of particles, DPMs are usually used to gain an insight into various vexing issues such as bubble or cluster formation and their characteristics or segregation phenomena. A few hundred thousand particles can be considered in such DPMs [3-5].

Taghipour et al. [6] have conducted experimental and computational studies of gas-solid fluidized bed reactor hydrodynamics. CFD simulation results were compared to those obtained from the experiments. A multifluid Eulerian model integrating the kinetic theory for solid particles was used for predicting the gas-solid behavior of a fluidized bed. Comparison of the model predictions, using the Syamlal-O'Brien, Gidaspow, and Wen-Yu drag functions, and experimental measurements on the time-average bed pressure drop, bed expansion, and qualitative gas-solid flow pattern indicated reasonable agreement for most operating conditions. Furthermore, the predicted instantaneous and time-averaged local voidage profiles showed similar trends with the experimental results.

Goldschmidt et al. [7] compared a hard-sphere discrete particle model with a two-fluid model containing kinetic theory closure equations using appropriate experimental data. Their results indicate that both CFD models predict adequate fluidization regimes and trends in bubble sizes and bed expansion, whereas predicted bed expansion dynamics differ significantly from the experimental results. Kaneko et al. [8] developed a DEM simulation code incorporated with the reaction and energy balances based on the soft sphere interaction at particle collision for a fluidized bed olefin polymerization. Heat transfer from particles to the gas was estimated by using the Ranz-Marshall equation. Their results were fairly realistic concerning particle and gas temperature behavior and also the bubbling behavior in a gas fluidized bed at elevated pressure. Behjat et al. [9] investigated unsteady state behavior of gas–solid fluidized

†To whom correspondence should be addressed.
E-mail: mahdi_hamzei@aut.ac.ir

beds. They showed that model predictions of bubble size and gas-solid flow pattern using both Syamlal-O'Brien and Gidaspow drag models were similar. Also, in their research when the bed containing two different solid phases was simulated, their results showed particles with smaller diameters had lower volume fraction at the bottom of the bed and higher volume fraction at the top of the Chamber.

Huilin et al. [10] studied a bubbling fluidized bed with the binary mixtures applying multifluid Eulerian CFD model according to the kinetic theory of granular flow. Their simulation results showed that the hydrodynamics of a gas bubbling fluidized bed is related to the distribution of particle sizes and the amount of dissipated energy in particle-particle interactions. Gobin et al. [11] numerically simulated a fluidized bed using two-phase flow method. In their work, time-dependent simulations were performed for industrial and pilot reactor operating conditions. The numerical predictions are in good qualitative agreement with the observed behavior in terms of bed height, pressure drop and mean flow regimes.

Lettieri et al. [12] used the Eulerian-Eulerian granular kinetic model available within the CFX-4 code to simulate the transition from bubbling to slugging fluidization for a typical Group B material at four fluidizing velocities. Results from simulations were analyzed in terms of voidage profiles and bubble size, which showed typical features of a slugging bed.

Although there have been many studies on the modeling and model evaluation of fluidized-bed hydrodynamics, only a few works have been published on the CFD modeling and model validation of combined reactor hydrodynamics and heat transfer. Also, only a limited number of works have been reported on the successful CFD modeling of fluidized bed hydrodynamics with heat transfer. In this research, heat transfer and hydrodynamics of two-dimensional non-reactive gas-solid fluidized bed chamber were experimentally and computationally studied. A multifluid Eulerian model incorporating the kinetic theory for solid particle was applied in order to simulate the gas-solid flow at different conditions. It is assumed that the inlet gas is cold (300 K) and the initial solid particle temperature is 340 K. To validate the model, simulation results were compared with the experimental data.

NUMERICAL PROCEDURES

1. Governing Equations

The governing equations of the system include the conservation of mass, momentum, and energy. Equations of solid and gas phases were developed based on Eulerian-Eulerian model using the averaging approach. The continuity equations for gas and solid phases without mass transfer between the phases, respectively, are [13,14]

$$\frac{\partial}{\partial t}(\varepsilon_g\rho_g)+\nabla\cdot(\varepsilon_g\rho_g\vec{v}_g)=0 \tag{1}$$

$$\frac{\partial}{\partial t}(\varepsilon_s\rho_s)+\nabla\cdot(\varepsilon_s\rho_s\vec{v}_s)=0 \tag{2}$$

By definition, the volume fractions of the phases must sum to 1:

$$\varepsilon_g+\varepsilon_s=1 \tag{3}$$

The conservation of momentum for the gas phase and solid phase is described by:

$$\frac{\partial}{\partial t}(\varepsilon_g\rho_g\vec{v}_g)+\nabla\cdot(\varepsilon_g\rho_g\vec{v}_g\vec{v}_g)=-\varepsilon_g\nabla P_g+\nabla\cdot\bar{\bar{\sigma}}_g+\varepsilon_g\rho_g\vec{g}+\beta_{gs}(\vec{v}_g-\vec{v}_s) \tag{4}$$

$$\frac{\partial}{\partial t}(\varepsilon_s\rho_s\vec{v}_s)+\nabla\cdot(\varepsilon_s\rho_s\vec{v}_s\vec{v}_s)=-\varepsilon_s\nabla P_s+\nabla\cdot\bar{\bar{\sigma}}_s+\varepsilon_s\rho_s\vec{g}+\beta_{gs}(\vec{v}_s-\vec{v}_g) \tag{5}$$

Where $\bar{\bar{\sigma}}$ is Reynolds stress tensor, p_s is the solids pressure, $(-\varepsilon_s\nabla p+\beta_{gs}(\vec{v}_g-\vec{v}_s))$ is an interaction force (drag and buoyancy forces) representing the momentum transfer between gas and solid phase and g is the gravitational constant, [15,16].

Several drag models exist for the gas-solid interphase exchange coefficient (β_{gs}). In this research the Syamlal-O'Brien drag model [17,18] was used. The drag law of Syamlal-O'Brien is based on the measurements of the terminal velocities of particles in fluidized or settling beds. The interphase exchange coefficient is expressed as

$$\beta_{gs}=\frac{3}{4}\frac{\varepsilon_s\varepsilon_g\rho_g}{v_{r,s}^2 d_s}C_D\left(\frac{Re_s}{v_{r,s}}\right)|\vec{v}_s-\vec{v}_g| \tag{6}$$

where C_D, the drag coefficient, is given by

$$C_D=\left(0.63+\frac{4.8}{\sqrt{Re_s/v_{r,s}}}\right)^2 \tag{7}$$

And $v_{r,s}$, a terminal velocity correlation, is expressed as

$$v_{r,s}=0.5(A-0.06Re_s+\sqrt{(0.06Re_s)^2+0.12Re_s(2B-A)+A^2}) \tag{8}$$

with $A=\varepsilon_g^{4.14}$ and

$$B=\begin{cases}0.8\varepsilon_g^{1.28} & \text{if } \varepsilon_g\le 0.85\\ \varepsilon_g^{2.65} & \text{if } \varepsilon_g>0.85\end{cases} \tag{9}$$

Also, the solid Reynolds number, Re_s, is calculated as

$$Re_s=\frac{\rho_g d_s|\vec{v}_g-\vec{v}_s|}{\mu_g} \tag{10}$$

The stress tensor for the gas phase assumed to be of the Newtonian form is given by

$$\bar{\bar{\sigma}}_g=-P_g\bar{\bar{I}}+2\varepsilon_g\mu_g\bar{\bar{D}}_g+\varepsilon_g\lambda_g tr(\bar{\bar{D}}_g)\bar{\bar{I}} \tag{11}$$

Where $\bar{\bar{I}}$ is the identity tensor and $\bar{\bar{D}}$ is the strain rate tensor for gas or solid phase, given by

$$\bar{\bar{D}}=\frac{1}{2}[\nabla\vec{v}+(\nabla\vec{v})^T] \tag{12}$$

Granular flows can be classified into two distinct flow regimes: a viscous or rapidly shearing regime, in which stresses arise because of collisional or translational transfer of momentum, and a plastic or slowly shearing regime, in which stresses arise because of friction between grains in enduring contact. In this work, a combination of viscous and plastic regime was applied to investigate the behavior of granular flow.

$$\bar{\bar{\sigma}}_s=\begin{cases}-P_s^p\bar{\bar{I}}+\bar{\bar{\tau}}_s^p & \text{if } \varepsilon_g\le\varepsilon_g^*\\ -P_s^v\bar{\bar{I}}+\bar{\bar{\tau}}_s^v & \text{if } \varepsilon_g>\varepsilon_g^*\end{cases} \tag{13}$$

$\bar{\bar{\tau}}_s$ is the viscous stress in the solid phase. The superscript p stands for plastic regime and v for viscous regime. In fluidized-bed simulations, ε_g^* is usually set to the void fraction at minimum fluidization [15].

The granular pressure is given by

$$P_s^v = K_1 \varepsilon_s^2 \Theta_s \tag{14}$$

Θ_s is the granular temperature of solid phase and K_1 is the granular stress constant that is given by

$$K_1 = 2(1+e_{ss})\rho g_{0,ss} \tag{15}$$

The granular stress is given by

$$\bar{\bar{\tau}}_s^v = 2\mu_s^v \bar{\bar{D}}_s + \lambda_s^v \mathrm{tr}(\bar{\bar{D}}_s)\bar{\bar{I}} \tag{16}$$

λ_s^v, the second coefficient of viscosity and μ_s^v, the shear viscosity for the solid phase, respectively, are given by

$$\lambda_s^v = K_2 \varepsilon_s \sqrt{\Theta_s} \tag{17}$$

$$\mu_s^v = K_3 \varepsilon_s \sqrt{\Theta_s} \tag{18}$$

Where

$$K_2 = \frac{4}{3\sqrt{\pi}} d_s \rho_s (1+e_{ss}) \varepsilon_s g_{0,ss} - \frac{2}{3} K_3 \tag{19}$$

And the constant K_3 is given by

$$K_3 = \frac{d_s \rho_s}{2}\left\{ \frac{\sqrt{\pi}}{3(3-e_{ss})}[1+0.4(1+e_{ss})(3e_{ss}-1)\alpha_s g_{0,ss}] + \frac{8\varepsilon_s g_{0,ss}(1+e_{ss})}{5\sqrt{\pi}} \right\} \tag{20}$$

$g_{0,ss}$ is the radial distribution function that for solid phase [8,22], use

$$g_{0,ss} = \left[1 - \left(\frac{\varepsilon_s}{\varepsilon_{s,max}} \right) \right]^{-1} \tag{21}$$

where e_{ss} is the coefficient of restitution for particle collisions and that is approximately constant.

Similar to the functions typically used in plastic flow theories, an arbitrary function that allows a certain amount of compressibility in the solid phase represents the solid pressure term for plastic flow regime:

$$P_s^p = \varepsilon_s P^* \tag{22}$$

where P^* is represented by an empirical power law:

$$P^* = 10^{25}(\varepsilon_g^* - \varepsilon_g)^{10} \tag{23}$$

A solids stress tensor based on the critical state theory is

$$\bar{\bar{\tau}}_s^p = 2\mu_s^p \bar{\bar{D}}_s \tag{24}$$

Where the shear viscosity for the solid phase in plastic flow is

$$\mu_s^p = \frac{P^* \sin\phi}{2\sqrt{I_{2D}}} \tag{25}$$

ϕ is the angle of internal friction, and I_{2D} is the second invariant of the deviatoric stress tensor [2,8,9,15,17].

$$I_{2D} = \frac{1}{6}[(D_{s11}-D_{s22})^2 + (D_{s22})^2 + (D_{s11})^2] + D_{s12}^2 \tag{26}$$

The granular temperature of solid phase (Θ_s) as an order of solid fluctuation is defined as one-third of the mean square velocity of particles' random motion. Granular energy is defined as the specific energy of solid particles' fluctuation. The following solid granular energy equation must be solved to calculate granular temperature [19,20].

$$\frac{3}{2}\frac{\partial}{\partial t}(\rho_s \varepsilon_s \Theta_s) + \frac{3}{2}\nabla\cdot(\rho_s \varepsilon_s \vec{v}_s \Theta_s) = \bar{\bar{\sigma}}_s : \nabla \cdot \vec{v}_s + \nabla\cdot(k_{\Theta_s}\nabla\Theta_s) - \gamma_{\Theta_s} - 3\beta_{gs}\Theta_s \tag{27}$$

where $\bar{\bar{\sigma}}_s : \nabla \cdot \vec{v}_s$ is the generation of energy by the solid stress tensor, $k_{\Theta_s}\nabla\Theta_s$ is the diffusion flux of granular energy (k_{Θ_s} is the diffusion coefficient). The collision dissipation of energy, γ_{Θ_s}, representing the rate of energy dissipation within the solid phase due to inelastic particle collisions that is derived by Lun et al. [20]

$$\gamma_{\Theta_s} = \frac{12(1-e_{ss}^2) g_{0,ss}}{d_s\sqrt{\pi}} \rho_s \varepsilon_s^2 \Theta_s^{3/2} \tag{28}$$

Also, the end term is the transfer of kinetic energy, due to random fluctuations in particle velocity.

In this work the following algebraic granular temperature equation was used with the assumptions that the granular energy is dissipated locally, the convection and diffusion contributions are negligible and only the generation and dissipation terms are retained [11,14]. When using this algebraic equation instead of solving the balance for the granular temperature, much faster convergence is obtained during simulations [13,14].

$$\Theta_s = \left\{ \frac{-K_1 \varepsilon_s \mathrm{tr}(\bar{\bar{D}}_s) + \sqrt{K_1^2 \mathrm{tr}^2(\bar{\bar{D}}_s)\varepsilon_s^2 + 4K_4[K_2 \mathrm{tr}^2(\bar{\bar{D}}_s) + 2K_s \mathrm{tr}(\bar{\bar{D}}_s^2)]}}{2\varepsilon_s K_4} \right\} \tag{29}$$

where K_4 is given by

$$K_4 = \frac{12(1-e_{ss}^2)\rho_s g_{0,ss}}{d_s\sqrt{\pi}} \tag{30}$$

k_{Θ_s} is the diffusion coefficient for granular energy. The Syamlal-O'Brien model is expressed as [17,18]

$$k_{\Theta_s} = \frac{15 d_s \rho_s \varepsilon_s \sqrt{\pi\Theta_s}}{4(41-33\eta)}\left[1 + \frac{12}{5}\eta^2(4\eta-3)\varepsilon_s g_{0,ss} + \frac{16}{15\pi}(41-33\eta)\eta\varepsilon_s g_{0,ss} \right] \tag{31}$$

With $\eta = \frac{1}{2}(1+e_{ss})$

The internal energy balance for the gas phase can be written in terms of the gas temperature as follows:

$$\varepsilon_g \rho_g Cp_g\left(\frac{\partial T_g}{\partial t} + v_g \cdot \nabla T_g\right) = -\nabla\cdot(\varepsilon_g k_g \nabla T_g) - H_{gs} \tag{32}$$

where k_g is the gas thermal conductivity. The solid heat conductivity includes direct conduction through the fractional contact area and indirect conduction through a wedge of the gas that is trapped between the particles.

The thermal energy balance for the solid phases is given by

$$\varepsilon_s\rho_s Cp_s\left(\frac{\partial T_s}{\partial t}+v_s\cdot\nabla T_s\right)=\nabla\cdot(\varepsilon_s k_s\nabla T_s)+H_{gs} \quad (33)$$

H_{gs} is the heat transfer between the gas and the solid is a function of temperature difference between the gas and solid phases.

$$H_{gs}=-\gamma^0_{gs}(T_s-T_g) \quad (34)$$

The heat transfer coefficient is related to the particle Nusselt number using the following equation.

$$\gamma^0_{gs}=\frac{6k_g\varepsilon_s Nu_s}{d_s^2} \quad (35)$$

The Nusselt number is determined by applying the following correlation. Re_s is the relative solid Reynolds number and Pr is the gas Prandtl number [8,9]

$$Nu_s=(7-10\varepsilon_g+5\varepsilon_g^2)(1+0.7Re_s^{0.2}Pr^{1/3})+(1.33-2.4\varepsilon_g+1.2\varepsilon_g^2)Re_s^{0.7}Pr^{1/3} \quad (36)$$

$$Pr=\frac{c_{p,s}\mu_g}{k_g} \quad (37)$$

2. Initial and Boundary Conditions

The initial values of the variables for all the fields (ε_g, ε_s, v_g, v_s) are specified for the entire computational domain. Initially, solid particle velocity was set at zero (in minimum fluidization), and gas velocity was assumed to have the same value everywhere in the bed. Initially, the temperature of solid phase was 340 K and also for gas phase set to 300 K. At the inlet, all velocities and volume fraction of all phases were specified. The outlet boundary condition was outward flow and was assumed to be fully developed flow. The gas tangential normal velocities on the wall were set to zero (no slip condition). The normal velocity of the particles was also set at zero. The following boundary equations apply for the tangential velocity and granular temperature of particles at the wall [21-23]:

$$\vec{v}_{s,w}=-\frac{6\mu_s\varepsilon_{s,max}}{\sqrt{3}\pi\rho_s\varepsilon_s g_{0,ss}\sqrt{\Theta_s}}\frac{\partial\vec{v}_{s,w}}{\partial n} \quad (38)$$

The general boundary condition for granular temperature at the wall takes the form

$$\Theta_{s,w}=-\frac{k_s\Theta_s}{e_{ss,w}}\frac{\partial\Theta_{s,w}}{\partial n}+\frac{\sqrt{3}\pi\rho_s\varepsilon_s v_s^2 g_o\Theta_s^{3/2}}{6\varepsilon_{s,max}e_{ss,w}} \quad (39)$$

Here $\vec{v}_{s,w}$ is the particle slip velocity, $e_{ss,w}$ is the restitution coefficient at the wall and $\varepsilon_{s,max}$ is the volume fraction for the particles at maximum packing. The boundary conditions for the energy equation are set such that the walls are adiabatic.

3. Computational Solution Procedure

The 2D computational domain is discretized by 4300 rectangular cells. A time step of 0.001 s with 20 iterations per time step is chosen. This iteration was adequate to achieve convergence for the majority of time steps. Governing equations of the system in unsteady state condition are solved by finite volume method employing the semi implicit method for pressure linked equations (SIMPLE) algorithm that is developed for multiphase flow using the partial elimination algorithm (PEA) [3,4]. The first-order upwind scheme was used for discretization of the equations. The conservation equations are integrated in the space and time. The sets of algebraic equations are solved iteratively [3,23,24]. The flowchart of the simulation algorithm for one time step is shown in Fig. 1.

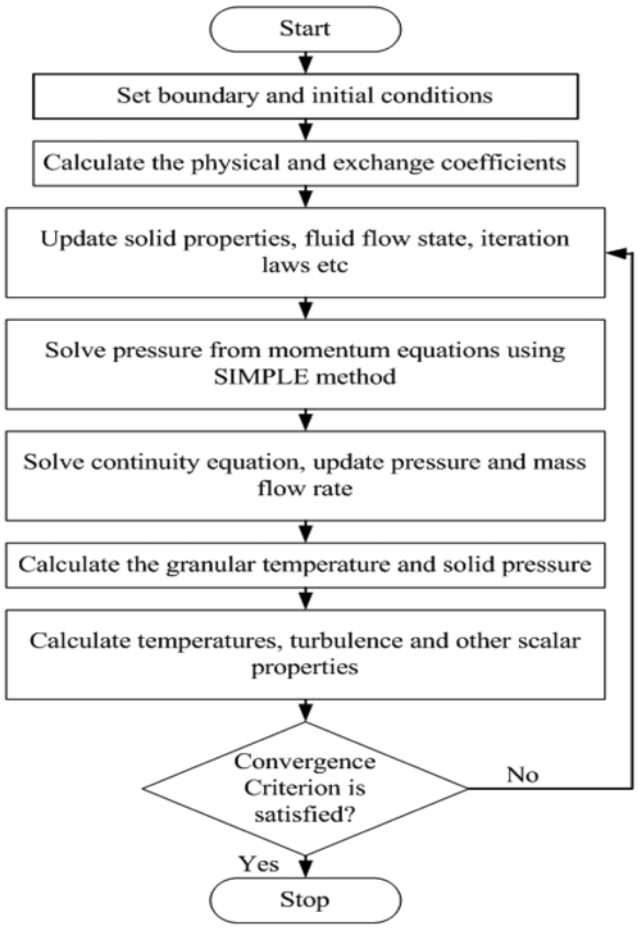

Fig. 1. Flowchart of the simulation procedure for one time step.

Sensitivity analysis of the effect the time step, mesh size, discretization schemes, and convergence criterion have on the results was also studied. The simulation results from the first-order discretization schemes for a time step of 0.001 s with 10^{-3} convergence criterion to second-order discretization schemes, for a time step of 0.0005 s, and 10^{-4} convergence criterion with 50 iteration at each time step show no noticeable difference in overall hydrodynamic behavior and temperature distribution among these simulations. Therefore, it is concluded the selected numerical parameters are adequate for proper simulations of bed hydrodynamic with heat transfer.

EXPERIMENTAL SETUP

Experiments were conducted in a Plexiglas cylinder of 40 cm height and 12 cm diameter. At the lower end of this is a distribution chamber and air distributor that supports the bed when defluidized. This distributor has been designed to ensure uniform airflow into the bed without causing excessive pressure drop and is suitable for

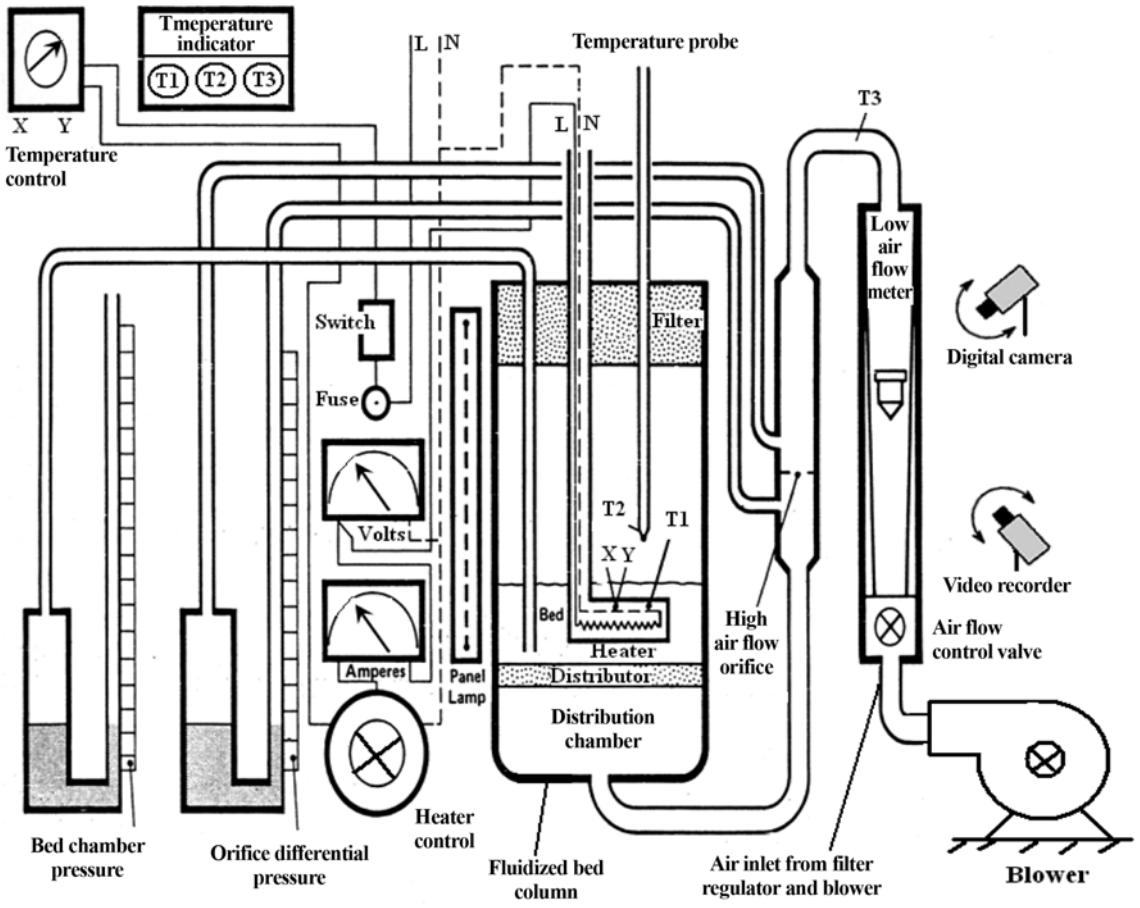

Fig. 2. A view of experimental set-up with its equipments.

Table 1. Values of model parameters used in the simulations and experiments

Description	Value	Comment
Solids density, ρ_s	1,183 kg/m^3	Alumina powder
Gas density, ρ_g	1.189 kg/m^3	Air at ambient temperature
Mean particle diameter, d_s	100 μm	Uniform distribution
Coefficient of restitution, e_{ss}	0.9	Fixed value
Initial solid packing	0.6	Fixed value
Fluidized bed diameter	12 cm	Fixed value
Fluidized bed height	40 cm	Fixed value
Initial static bed height	15 cm	Fixed values
Superficial gas velocity	0-10 cm/s	A range value
Initial temperature of solid	340 K	Fixed value
Inlet gas temperature	300 K	Fixed value
Maximum solids packing, ε_{max}	0.61	Syamlal et al. [17,18]
Angle of internal friction, ϕ	30°	Johnson and Jackson [22]
Inlet boundary conditions	Velocity	Superficial gas velocity
Outlet boundary conditions	Out flow	Fully developed flow

the granular material supplied. Spherical particles of 100 μm diameter and 1,183 kg/m^3 density were fluidized with air at ambient conditions. The initial static bed height was 15 cm with a solids volume fraction of 0.6. A Roots-type blower supplied the fluidizing gas. A pressure-reducing valve was installed to avoid pressure oscillations and to achieve a steady gas flow. Upon leaving the bed, the air passes through the chamber and escapes to the atmosphere through a filter. Installed in the bracket are probes for temperature and pressure measurement, and a horizontal cylindrical heating element, all of which may move vertically to any level in the bed chamber. Air is delivered through a filter, pressure regulator and an air flow meter fitted with a control valve and an orifice plate (to measure higher flow rates), to the distribution chamber. The heat transfer rate from the heating element is controlled by a variable transformer, and the voltage and current taken are displayed on the panel. Two thermocouples are embedded in the surface of the element. One of these indicates the surface temperature and the other, in conjunction with a controller, prevents the element temperature from exceeding a set value. A digital temperature indicator with a selector displays the temperatures of the element, the air supply to the distributor, and the moveable probe in the bed chamber. Two liquid filled manometers are fitted. One displays the pressure of the air at any level in the bed chamber, and the other displays the orifice differential pressure, from which the higher air flow rates can be determined. Pressure fluctuations in the bed are obtained by two pressure transducers that are installed at the lower and upper level of the column. The electrical heater increases the solid particle temperature, so the initial solid particle temperature was 340 K and for inlet air was 300 K (atmospheric condition). The ratio of the distributor pressure drop

to the bed pressure drop exceeded 14% for all operating conditions investigated.

RESULTS AND DISCUSSION

Simulation results were compared with the experimental data in order to validate the model. The pressure drop was experimentally measured for different gas velocities and compared with those predicted by CFD simulation.

As indicated in Fig. 3, the bed overall pressure drop significantly decreased at the beginning of fluidization and then fluctuated around a near steady-state value after about 3.5 s. Pressure drop fluctuations are expected as bubbles continuously split and coalesce in a transient manner in the fluidized bed. Comparison of the model predictions, using the Syamlal-O'Brien drag functions and experimental measurements on pressure drop and the time-average bed, indicated that good agreement exists at most operating conditions. These results are the same as those reported by Tagipour et al. [6] and Behjat et al. [9].

A comparison of the time-average bed pressure drop, using the Syamlal-O'Brien drag functions, against superficial gas velocity is plotted in Fig. 4. The results show that with increasing the gas velocity, the pressure drop increases. The simulation and experimental results show better agreement at velocities above U_{mf} (2.2 cm/s). The discrepancy for $U<U_{mf}$ may be attributed to the solids not being fluidized, thus being dominated by interparticle frictional forces, which are not predicted by the multifluid model for simulating gas-solid phases.

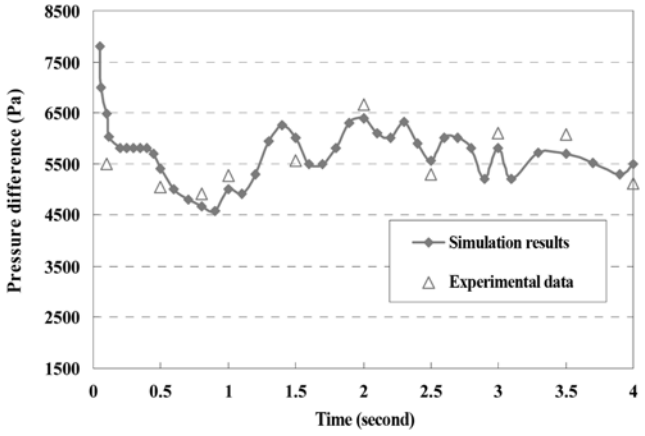

Fig. 3. Comparison of experimental and simulation bed pressure difference versus time.

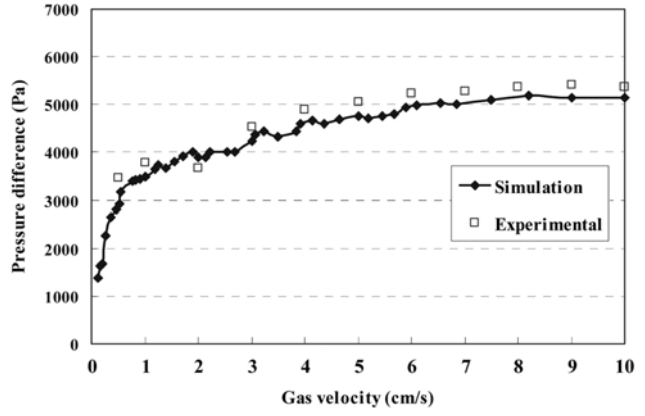

Fig. 4. Comparison of experimental and simulated bed pressure drop at different gas velocities.

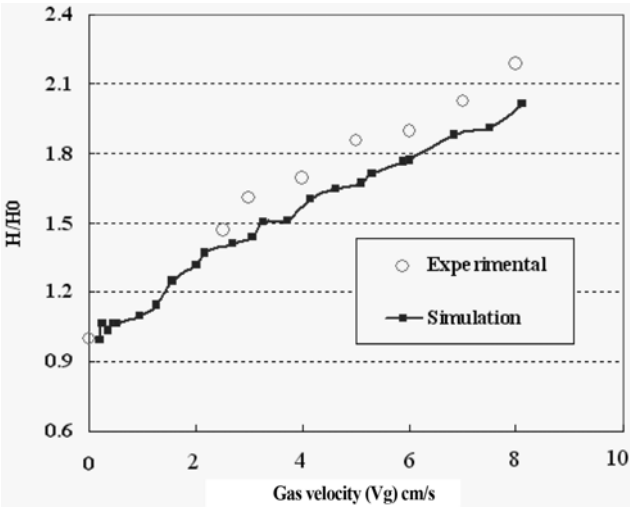

Fig. 5. Comparison of experimental and simulated bed expansion ratio.

The experimental data and simulation results for time-average bed expansions as a function of superficial velocities are compared in Fig. 5. It shows that the models predict the correct increasing trend of the bed height with the increase of superficial gas velocity. Good agreement has been observed between the model predictions and the experimental data for bed expansion ratio and qualitative gas-solid flow patterns. Similar trends were reported for pressure drop and bed expansion in the earlier works [5,6,9,17,18].

Fig. 6 shows simulation results for solid volume fraction contour plot for V_g=6 cm/s. An increase in bed expansion and variation of the fluid-bed voidage can be observed. At the start of the simulation, waves of voidage are created, which travel through the bed and subsequently break to form bubbles as the simulation progresses. Initially, the bed height increased with bubble formation until it leveled off at a steady-state bed height. The observed axi-symmetry gave way to chaotic transient generation of bubble formation after 1.5 s.

The bubbles coalesce as they move upwards producing bigger bubbles. The bubbles become stretched because of bed wall effect and interactions with other bubbles. The results indicate similarities between the simulation and experiment at t=2 s. The simulation indicated small bubbles near the bottom of the bed; the bubbles grew as they rose to the top surface with coalescence. The elongation of the bubbles was due to wall effects and interaction with other bubbles. The Syamlal-O'Brien drag model provided similar qualitative flow patterns. The size of the bubbles predicted by the CFD models are in general similar to those observed experimentally. Fig. 7 compares experimental results for bubble formation and bed expansion for different superficial gas velocities. At low gas velocities, the solids rest on the gas distributor and the column is in the fixed bed regime. When superficial gas velocity reaches the fluidization veloc-

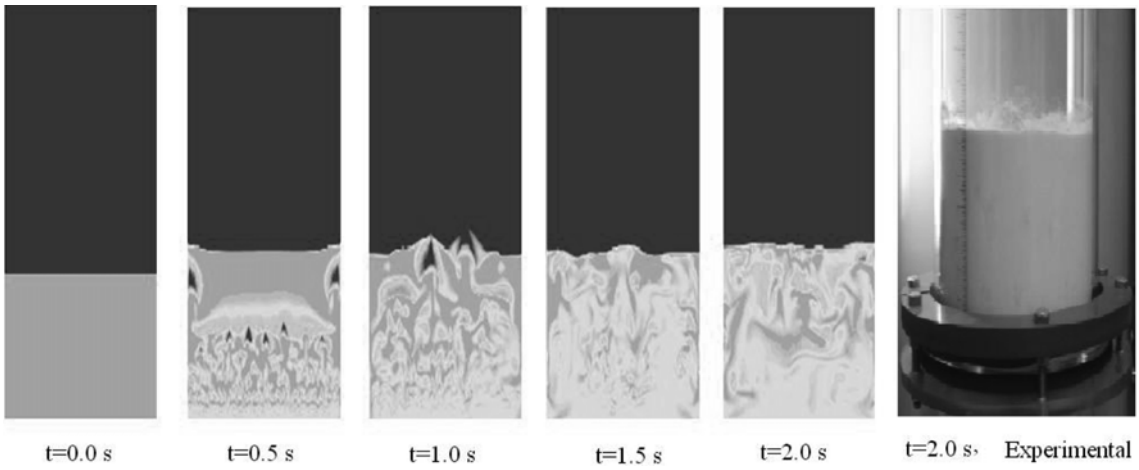

Fig. 6. Simulated gas volume fraction, void fraction, profile of 2D bed and experimental result (V_g=6 cm/s).

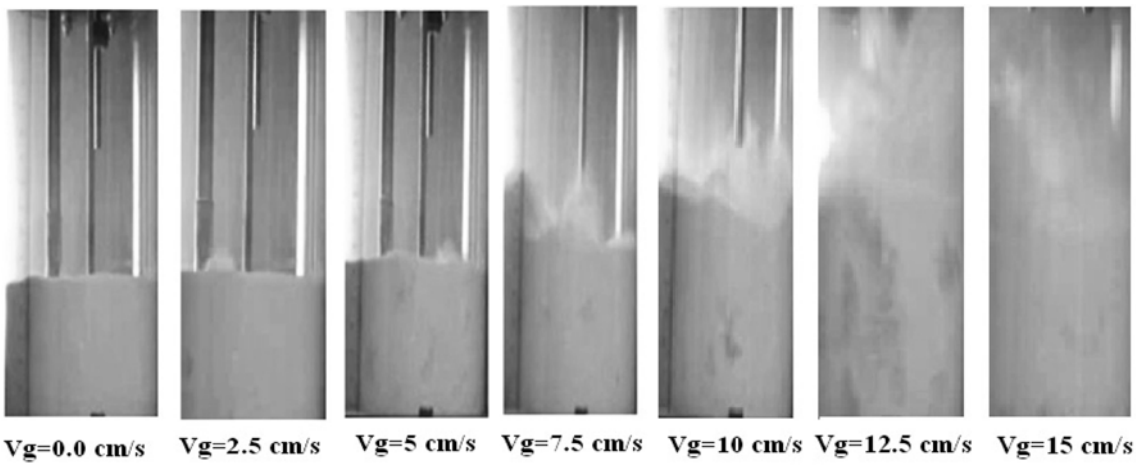

Fig. 7. Comparison of bubble formation and bed expansion for different superficial gas velocities.

ity, all particles are suspended by upward flowing gas and the bed is fluidized. Also, the bubbles are formed in the bed that are moved to the upper part of the column.

At this point, the gas drag force on the particle counterbalances the weight of the particle. If the gas velocity increases beyond the minimum fluidization velocity, smooth fluidization forms in the bed (for fine solids) up to a certain velocity limit. With an increase in velocity beyond minimum bubbling velocity, large instabilities with bubbling and channeling of gas are observed. At high gas velocities, the movement of solids becomes more vigorous. Such a bed is called a bubbling bed or heterogeneous fluidized bed, in this regime; gas bubbles generated at the distributor coalesce and grow as they rise through the bed.

In addition, with increasing the gas velocity, bubble formation and bubble collapse increase rapidly. Fig. 8 shows the simulation results of gas volume fraction for different gas velocities. Initially, the bed height increases with bubble formation so gas volume fraction increases and is leveled off at a steady-state bed height. At the start of the simulation, waves of voidage are created, which travel through the bed and subsequently break to form bubbles as the simulation progresses.

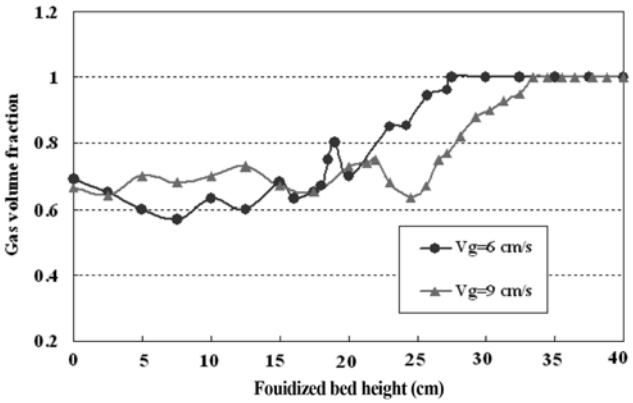

Fig. 8. Simulation results of gas volume fraction (t=7 s).

At the bottom of column, the concentration of particles is more than the upper part. Therefore, the maximum gas volume fraction occurs at the top level in the column. Clearly, the gas volume fraction of 1 (above the bed) corresponds to the region in the absence of particles.

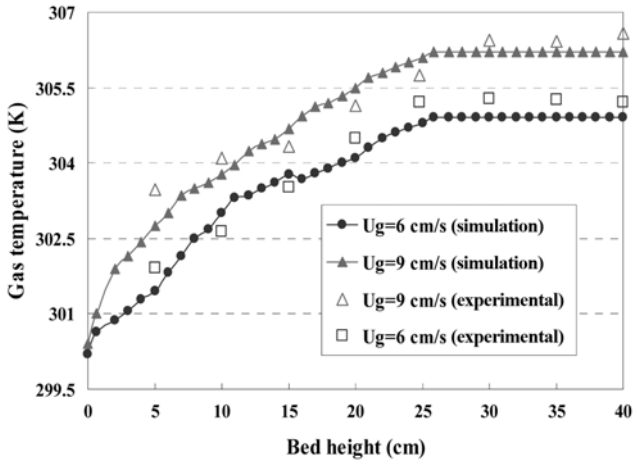

Fig. 9. Comparison of experimental and numerical results of gas temperature at different gas velocities (t=7 s).

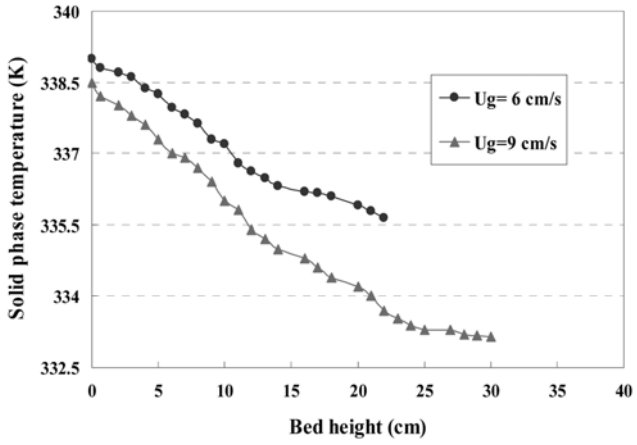

Fig. 11. Simulation results for variation of solid phase temperature at different gas velocity (t=7 s).

The gas mean temperatures as function of height for t=7 s are presented in Fig. 9. The gas temperature increases with height because of the heat transfer between the hot particles and cold gas. Near the bottom of the column, the solid volume fraction is relatively high; therefore, the gas temperature increases rapidly and the increase rate is higher for the region near the bottom of the column. At the top of the column, there are no particles (gas volume fraction is one) and the wall is adiabatic; therefore, the gas temperature is roughly constant. Also, the results show that with increasing the gas velocity, as expected the gas temperature increases.

Also, the variation of gas temperature in the column at two different inlet gas velocities is shown in this figure. It indicates that an increase in the gas velocity, due to a higher heat transfer coefficient between gas and solid phases, leads to a higher gas temperature because the initial temperature of solid particles was 340 K and for inlet gas it was 300 K. Also, the temperature gradient between solid and gas phases is lower at the top of the bed which leads to a lower heat transfer rate compared to the bottom of the bed.

The simulation results for gas temperature are in good agreement with the experimental data. The small differences seen are the result of the slight heat loss from the wall in the experimental column.

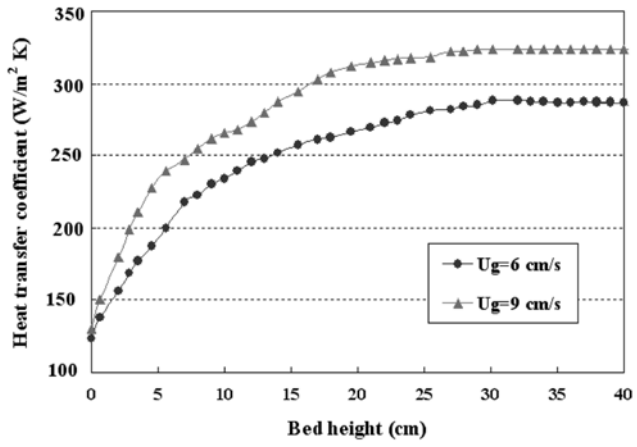

Fig. 10. Simulation results for heat transfer coefficient at different gas velocities (t=7 s).

Simulation results for heat transfer coefficient at different gas velocities at t=7 s are shown in Fig. 10. From the results of this figure, the heat transfer coefficient increases from bottom to top in the column because with results of Fig. 8. Gas volume fraction increases from bottom to top. This figure also indicates that an increase in the gas velocity causes a higher heat transfer coefficient between gas and solid phases.

The effect of inlet gas velocity on solid phase temperature is shown in Fig. 11. It indicates that an increase in gas velocity causes a higher heat transfer leading to an increase in solid particle temperature and in a decrease in gas temperature. Temperature distribution predicted by the simulations was in good agreement with experimental measurements. Furthermore, the comparison between experimental and computational simulation showed that the model could predict hydrodynamic and heat transfer behavior of the fluidized bed reasonably well.

Simulation results for the heat transfer coefficient (Fig. 10) were in good agreement with the gas and solid temperature results (Fig. 9 and Fig. 11). The results show that with increasing the gas velocity, as expected the gas temperature increases (Fig. 9) and solid particles temperature decreases (Fig. 9). In addition, the gas temperature increases or solid particle temperature decreases with height because of the heat transfer between the hot particles and cold gas.

CONCLUSION

Unsteady state heat transfer and hydrodynamics in a gas-solid fluidized bed reactor have been investigated. Preliminary investigation of multiphase flow models revealed that the Eulerian-Eulerian model is suitable for modeling of industrial fluidized bed reactors. The model includes continuity equations, momentum and energy equations for both phases and the equations for granular temperature of solid particles. A suitable numerical method that employs finite volume method has been applied to discretize the equations. Simulation results also indicated that small bubbles were produced at the bottom of the bed. These bubbles collided with each other as they moved upwards forming larger bubbles. The influence of solid

particle temperature on the gas temperature was studied. The results indicated that with increasing the gas velocity, due to a higher heat transfer coefficient between the gas and the solid phase, solid phase temperature decreases and the mean gas temperature increases, both rapidly. To validate the model, the predicted pressure drops and gas temperature variations were compared with the corresponding values of experimental data. The modeling predictions compared reasonably well with the experimental data. Furthermore, this comparison showed that the model could predict hydrodynamic and heat transfer behavior of a gas solid fluidized bed reasonably well.

ACKNOWLEDGMENTS

The authors would like to express their gratitude to the Fluid Mechanics Research Center in the Department of Mechanical Engineering of Amirkabir University and Petrochemistry Research and Technology Company for providing financial support for this study.

NOMENCLATURE

C_D : drag coefficient [-]
$\underline{Cp}$: specific heat [kj/kg·k]
$\overline{\overline{D}}_s$: solids strain rate tensor [s^{-1}]
d_s : solid diameter [mm]
e_{ss} : coefficient of restitution of particle [-]
g : gravitational constant [9.81 m/s^{-2}]
$g_{0,ss}$: radial distribution function [-]
H_{gs} : heat transfer between the gas and the solid
I_{2D} : second invariant of the deviatoric stress tensor [-]
k : thermal conductivity
k_{Θ_s} : diffusion coefficient for granular energy [kg/s m]
Nu : nusselt number [-]
P : pressure [Pa]
Pr : gas prandtl number [-]
Re : reynolds number [-]
$\overline{\overline{s}}$: stress tensor [Pa]
T : thermodynamic temperature [K]
U_g : superficial gas velocity [m/s]
V : velocity [m/s]
$\vec{V}_{s,\parallel}$: particle slip velocity parallel to the wall [m/s]
v_{rs} : terminal velocity correlation [m/s]

Greek Letters

γ_{Θ_s} : collision dissipation of energy [kg/s^3m]
β_{gs} : gas-solid inter phase exchange coefficient [-]
ε : volume fraction [-]
$\varepsilon_{s,max}$: volume fraction for the particles at maximum packing [-]
Θ : granular temperature [m^2/s^2]
λ : second coefficient of viscosity [kg/m·s]
μ : viscosity [kg/m·s]
$\overline{\overline{\tau}}$: reynolds stress tensor [Pa]
ρ : density [kg/m^3]
ϕ : angle of internal friction [-]
$\overline{\overline{\sigma}}$: stress tensor [Pa]
ϕ_{gs} : transfer of kinetic energy [kg/s^3m]

Subscripts

g : gas
mf : minimum fluidization
s : solids

Superscripts

p : plastic regime
v : viscous regime

REFRENCES

1. D. Kunii and O. Levenspiel, *Fluidization engineering*, Butterworth-Heinemann Publications, Boston (1991).
2. D. Gidaspow, *Multiphase flow and fluidization*, Academic Press, London (1994).
3. V. V. Ranade, *Computational flow modeling for chemical reactor engineering*, Academic Press, New York (2002).
4. R. B. Bird, W. E. Stewart and E. N. Lightfoot, *Transport phenomena*, Wiley Publications, New York (2002).
5. J. R. Grace and F. Taghipour, *Powder Technol.*, **139**, 99 (2004).
6. F. Taghipour, N. Ellis and C. Wong, *Chem. Eng. Sci.*, **60**, 6857 (2005).
7. M. J. V. Goldschmidt, J. A. M. Kuipers and W. P. M. Van Swaaij, *Chem. Eng. Sci.*, **56**, 571 (2001).
8. Y. Kaneko, T. Shiojima and M. Horio, *Chem. Eng. Sci.*, **54**, 5809 (1999).
9. Y. Behjat., S. Shahhosseini and S. H. Hashemabadi, *Int. Commun. Heat. Mass.*, **35**, 357 (2008).
10. L. Huilin, H. Yurong and D. Gidaspow, *Chem. Eng. Sci.*, **58** 1197 (2003).
11. H. Gobin, O. Neau, J. Simonin, V. Llinas and J. L. Reiling, *Int. J. Numer. Meth. Fl.*, **43**, 1199 (2003).
12. P. Lettieri, G. Saccone and L. Cammarata, *Chem. Eng. Res. Des.*, **82**, 939 (2004).
13. M. Chiesa, V. Mathiesen, J. A. Melheim and B. Halvorsen, *Comput. Chem. Eng.*, **29**, 291 (2005).
14. B. G. M. Van Wachem, J. C. Schouterf, R. Krishnab and V. Bleek, *Comput. Chem. Eng.*, **22**, 299 (1998).
15. R. Fan and R. O. Fox, *Chem. Eng. Sci.*, **63**, 272 (2008).
16. Z. Mansoori, M. Saffar-Avval, H. Basirat Tabrizi and G. Ahmadi, *Int. J. Heat. Mass. Tran.*, **45**, 1173 (2002).
17. M. Syamlal and T. J. O'Brien, *AIChE J.*, **85**, 22 (1989).
18. M. Syamlal and T. J. O'Brien, *AIChE J.*, **49**, 2793 (2003).
19. I. K. Gamwo, Y. Soong and R. W. Lyczkowski, *Powder Technol.*, **103**, 117 (1999).
20. C. K. K. Lun and S. B. A. Savage, *J. Appl. Mech.*, **54**, 47 (1987).
21. K. Hui, P. K. Haff and R. Jackson, *J. Fluid. Mech.*, **145**, 223 (1984).
22. P. C. Johnson and R. Jackson, *J. Fluid. Mech.*, **176**, 67 (1987).
23. S. V. Patankar, *Numerical heat transfer and fluid flow*, Hemisphere Publications, Washington DC (1980).
24. M. Hamzehei and H. Rahimzadeh, *Ind. Eng. Chem. Res.*, **48**, 3177 (2009).